Validation and Interpretation of a Three-dimensional Configuration of a Magnetic Cloud Flux Rope

Qiang Hu[1] , Chunming Zhu[2] , Wen He[3], Jiong Qiu[2] , Lan K. Jian[4] , and Avijeet Prasad[5,6]

[1] Department of Space Science and Center for Space Plasma and Aeronomic Research (CSPAR) The University of Alabama in Huntsville Huntsville, AL 35805, USA; qiang.hu@uah.edu, qiang.hu.th@dartmouth.edu
[2] Physics Department, Montana State University, Bozeman, MT 59717, USA
[3] Department of Space Science, The University of Alabama in Huntsville, Huntsville, AL 35805, USA
[4] Heliophysics Science Division, NASA Goddard Space Flight Center, Greenbelt, MD 20771, USA
[5] Institute of Theoretical Astrophysics, University of Oslo, Postboks 1029 Blindern, NO-0315 Oslo, Norway
[6] Rosseland Centre for Solar Physics, University of Oslo, Postboks 1029 Blindern, NO-0315 Oslo, Norway

Abstract

One *strong* magnetic cloud (MC) with a magnetic field magnitude reaching ∼40 nT at 1 au during 2012 June 16–17 is examined in association with a preexisting magnetic flux rope (MFR) identified on the Sun. The MC is characterized by a quasi-three-dimensional (3D) flux rope model based on in situ measurements from the Wind spacecraft. The contents of the magnetic flux and other parameters are quantified. In addition, a correlative study with the corresponding measurements of the same structure crossed by the Venus Express (VEX) spacecraft at a heliocentric distance of 0.7 au and with an angular separation of ∼6° in longitude is performed to validate the MC modeling results. The spatial variation between the Wind and VEX magnetic field measurements is attributed to the 3D configuration of the structure appearing as a knotted bundle of flux. A comparison of the magnetic flux contents between the MC and the preexisting MFR on the Sun indicates that the 3D reconnection process accompanying an M1.9 flare may correspond to the magnetic reconnection between the field lines of the preexisting MFR rooted in the opposite polarity footpoints. Such a process reduces the amount of the axial magnetic flux in the erupted flux rope, by approximately 50%, in this case.

1. Introduction

Coronal mass ejections (CMEs) are one important type of solar eruption that are closely related to solar flares. They can have long-lasting impacts that may manifest throughout the interplanetary space. Both remote-sensing and in situ spacecraft observations are available during the initiation, eruption, and propagation stages of a CME (and sometimes the accompanying flare). When a CME reaches the interplanetary space, it is called an interplanetary CME (ICME) with a variety of distinctive signatures present in the in situ data (Zurbuchen & Richardson 2006). The magnetic field structure embedded or hypothesized to have formed at the early stages of a CME eruption is believed to be directly associated with the various manifestations of the corresponding flare/CME evolution and eruptions.

A magnetic flux rope (MFR) is generally believed to form the core structure of a CME eruption (e.g., Vourlidas 2014; Amari et al. 2018; Liu 2020; Jiang et al. 2021b). However, the existence or the formation of such a structure on the Sun has yet to be fully elucidated. A clear definition for an MFR, either intuitively or preferably based on magnetic field properties, has to be articulated and agreed upon. Admittedly, despite many indirect observational signatures of MFRs on the Sun (e.g., Liu 2020), it remains challenging for direct magnetic field measurements of an MFR, especially in the corona. On the

other hand, such direct measurements are available in the interplanetary space, taken when an ICME encounters an observing spacecraft. In particular, one class of ICMEs, the so-called magnetic clouds (MCs), possesses a unique set of signatures in the in situ magnetic field and plasma parameters (Burlaga et al. 1982; Burlaga 1988, 1991): (1) enhanced magnetic field magnitude, (2) smooth/gradual rotation in one or more components of the magnetic field, and (3) depressed proton temperature or β value (the ratio between the plasma pressure and the magnetic pressure). Given these signatures and the fact that the spacecraft traverses the body of an MC structure, a flux rope configuration has been hypothesized to characterize the magnetic field structure of an MC since early times (e.g., Gosling 1990).

Based on in situ quantitative measurements and the flux rope hypothesis, various models have been devised to fit the data. Among them, an early and commonly used one is based on a cylindrically symmetric linear force-free field (LFFF) configuration described by a simple analytic solution, the so-called Lundquist solution (Lundquist 1950). The justification for an LFFF formulation is provided by the usually small β ($\ll 1$) for an MC interval. The Lundquist solution represents a type of one-dimensional (1D) model that only has a spatial dependence on the radial distance from the cylindrical axis. Being the earliest quantitative approach, the Lundquist solution model has been widely applied to fit the magnetic field profiles from in situ measurements of MCs (e.g., Burlaga 1988; Lepping et al. 1990; Wu et al. 2021). An alternative and unique two-dimensional (2D) model was later developed and applied to MC/ICME events, based on the Grad–Shafranov (GS)

equation describing a 2D magnetohydrostatic equilibrium (Hu & Sonnerup 2001, 2002; Hu 2017). In the GS-based method, the force-free condition is no longer needed, and the solution is fully 2D over a cross-section plane that does not change along the third (axial) dimension in the direction perpendicular to the plane.

To complement and overcome the limitation of the 2D geometry of the GS reconstruction, we recently adopted a quasi-three-dimensional (3D) model based on a more general LFFF formulation (Freidberg 2014), which introduces much greater spatial variation than the Lundquist solution. The approach is to fit such an analytic model to in situ spacecraft measurements of the magnetic field components with uncertainty estimates (typically on the order of 1 nT on average for data at 1 au) through a formal least-squares χ^2 minimization algorithm (Press et al. 2007; Hu et al. 2021a; Hu 2021). The fitting results with a minimum reduced χ^2 value of around 1 are considered optimal, together with a set of geometrical and physical parameters characterizing a flux rope configuration with 3D features. It has been shown that the field lines exhibit typical twists along one dimension, as well as apparent writhe, in the form of the overall winding of a flux bundle corresponding to one major polarity. There are also cases of two bundles of mixed (opposite) polarities winding around each other (Hu et al. 2021a). Such a model complements the existing GS method and allows us to perform MC analysis with an additional tool, and thus expand our MC event databases. In addition to the added features of a 3D configuration, the 3D model also tends to enable the selection of a larger MC interval for analysis as compared with that of the 2D GS method to better reconstruct the underlying structure in its entirety.

Since in situ MC modelings are nearly all based on single-point (or equivalently single-line) measurements across an MC structure, the validation of the model output is not always within reach. One way is to use more than one set of in situ spacecraft measurements obtained when the structure traverses multiple (often two) spacecraft with appropriate separation distances. Then the modeling result derived from one spacecraft data set can be used to produce a *prediction* or the expected values of the magnetic field along the path of the other spacecraft across the same structure. Such predicted values then can be compared with the actual measured ones to provide validation of the MC model. Such occasions are generally rare and such a validation approach has been carried out for the 2D GS reconstructions of a handful of MC events (Hu et al. 2005; Möstl et al. 2008, 2009). The latest applications to the quasi-3D model outputs have been performed as well (Hu et al. 2021b; Hu 2021). For example, in Hu et al. (2021b) an MC structure was observed by both the Solar Orbiter (SO) at a heliocentric distance of ∼0.8 au and the Wind spacecraft at Earth with a longitudinal separation angle of ∼4°. The analyses of the MC structure with both the 2D GS reconstruction and the quasi-3D model fitting were carried out by using the Wind spacecraft measurements and the expected values of the magnetic field along the SO spacecraft path were produced for both models. A comparison with the actual measurements at SO yielded a linear correlation coefficient >0.9 for both methods. In Hu (2021), a similar validation study for the quasi-3D model between the Advanced Composition Explorer (ACE) and the Solar and TErrestrial RElations Observatory (STEREO) B spacecraft, separated by ∼3° in longitude near 1 au, yielded a correlation coefficient of 0.89.

The other method of validation, still employing multi-spacecraft measurements, is to relate the in situ MC flux rope properties with their counterparts in the corresponding solar source regions derived from multiwavelength remote-sensing observations. Early attempts, through rigorous quantitative analyses of both in situ MCs by the 2D GS method and the corresponding source region properties in terms of the magnetic flux contents have been made by Qiu et al. (2007) and Hu et al. (2014) for about two dozen events with flare-CME-ICME/MC associations. It was found that the magnetic flux contents of MCs in terms of the toroidal (axial) and the poloidal flux correlate with the magnetic reconnection flux derived from the accompanying flare ribbon observations (Qiu et al. 2004, 2010). In particular, the comparison between the poloidal flux and the reconnection flux exhibits a one-to-one correspondence (Hu et al. 2014; Gopalswamy et al. 2017). Additional case studies also followed to further relate the axial flux contents in MCs to their source regions, either with or without the direct identification of the corresponding MFR footpoints on the Sun (Wang et al. 2017; Xing et al. 2020). These results support the scenarios envisaged by Longcope & Beveridge (2007) and Priest & Longcope (2017) (see, also, van Ballegooijen & Martens 1989) of MFR formation via sequential magnetic reconnection between sheared magnetic loops, often manifested as *two-ribbon* flares. During the process, the reconnection flux is largely injected into the ensuing MFR forming above the flare loops and ejected with the CME eruption. The brightened flare ribbons map the footpoints of reconnected field lines. Combined with the corresponding magnetograms, the amount of magnetic flux encompassed by the ribbon areas (equivalent to the reconnection flux) can be measured routinely through standardized procedures (e.g., Kazachenko et al. 2017). Such quantitative intercomparison not only provides insight into the MFR formation on the Sun, but also results in (indirect) validation of the in situ MC modeling results, given an implied consistency with certain theoretical frameworks. In the above-mentioned works, the scenario of an MFR formation through magnetic reconnection is supported by the analysis result that the amount of reconnection flux corresponds well to the poloidal flux of the MFR with an approximate 2D geometry.

Needless to say, the complexity in the modeling of solar source region magnetic field topology has outpaced the in situ modeling of MCs. We attempt to develop and apply a more complex model that is on a par in complexity with the source region magnetic field topology, and to explore connections with more nonstandard processes that go beyond a standard view, e.g., under an approximate 2D geometry, for flare-associated reconnection. For example, Aulanier & Dudík (2019) described magnetic reconnection processes in 3D geometries that may involve more complex changes in field-line topology and connectivity. In particular, they illustrated a process of magnetic reconnection between the two legs of an MFR, resulting in a removal of the axial flux. This process is distinctive from a standard tether-cutting type reconnection, which increases the flux as described earlier, although it also forms a similar set of flare loops (and ribbons). The motivation of the current study is twofold: (1) to validate the quasi-3D MC model by employing the aforementioned validation approaches, and (2) to relate to the solar source region MFR properties involving possible 3D reconnection processes mentioned here. Therefore, we aim to study another view on

flare-CME-ICME connection based on an alternative interpretation of the results of the analysis of one particular event.

We select the solar event on 2012 June 14 (SOL2012-06-14) for the present study. The sequence of events includes a series of confined C-class flares preceding the main M1.9 flare, followed by the accompanying CME eruption. The corresponding remote-sensing observations are obtained from the Solar Dynamics Observatory (SDO), including Atmospheric Imaging Assembly (AIA) and Helioseismic and Magnetic Imager (HMI), and the coronagraphs on board the Solar and Heliospheric Observatory (SOHO) and STEREO spacecraft. They have been analyzed by Wang et al. (2019) and Zhu et al. (2020) in great detail. Several hours prior to the eruptions, an MFR structure was inferred from conjugate dimming signatures and both footpoint regions were clearly identified and found to be rooted in strong and opposite magnetic polarity regions with strong vertical currents (Wang et al. 2019). This preexisting MFR prior to the main flare and CME eruptions was found to have been formed via a sequence of reconnections facilitated by photospheric and coronal evolution processes (see, also James et al. 2017). Its magnetic properties were derived by Wang et al. (2019) and will be compared with our in situ modeling results. The erupted CME reached Earth on June 16 and lasted for about a day as observed by the Wind spacecraft. Around that time period, the Venus Express (VEX) spacecraft at Venus was in approximate radial alignment with Earth and detected the same ICME/MC structure, thus providing an additional set of in situ measurements (magnetic field only; Zhang et al. 2006) for the validation study. In what follows, we will present a unique analysis of the MC structure by the quasi-3D model based on the Wind spacecraft measurements, complemented with a correlative study with the corresponding VEX measurements. Based on these new results of in situ analysis and their connection to the source region properties, mainly associated with the preexisting MFR and the measured reconnection flux, we offer an interpretation of the evolution of the MFR topology upon eruption, on the basis of a quantitative analysis of the derived toroidal (or axial) magnetic flux, which is still well characterized under 3D geometries. And increasingly it has been well quantified from solar observations (e.g., Xing et al. 2020).

This paper is organized as follows. In Section 2, we present an overview of the event, including the timelines for the associated flare, CME, and ICME, based on prior works and focus on in situ measurements and identification of an MC interval. We present the new modeling results for the MC by applying the quasi-3D model to the in situ Wind spacecraft data. In particular, a correlative study with the corresponding VEX in situ measurements is performed. We relate the in situ MC modeling results with the solar MFR properties in Section 3 and offer an interpretation of such a quantitative connection. Finally, we conclude in the last section.

2. Event Overview and In Situ MC Model Result

### 2.1. Event Overview and In Situ Measurements

The flare-CME event on 2012 June 14 has been well studied and the observational analyses of remote-sensing measurements have been conducted and reported in several prior studies (e.g., Wang et al. 2019). In particular, James et al. (2017, and references therein) have thoroughly examined the association among the flares, CME, and the corresponding
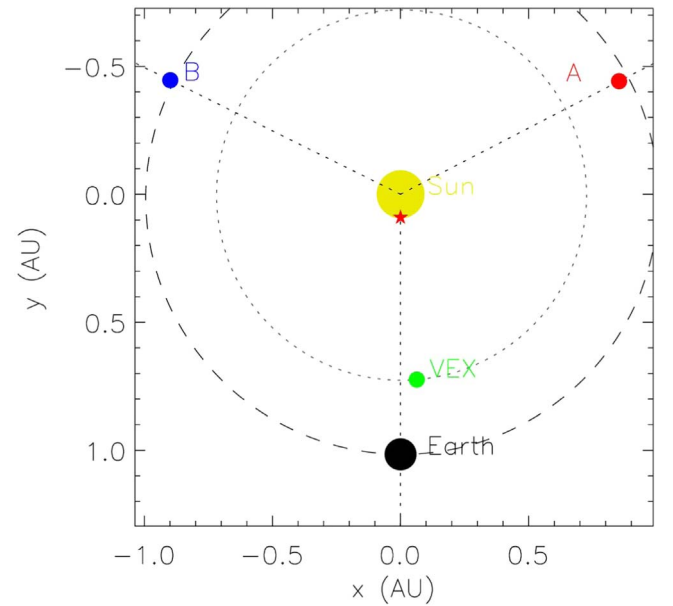

Figure 1. The spacecraft locations projected on the ecliptic plane on 2012 June 14: STEREO A and B, VEX, and Wind (Earth), as denoted. The red star indicates the approximate location of the solar source region of the flare/CME eruption (Earth facing in this case).

ICME with a set of comprehensive remote-sensing observations including UV/EUV, coronagraphic, and microwave imagery. We refer readers to those references for details and only provide a brief summary of the event sequence, but focus on in situ measurements and MC modeling in this section. The pair of an M1.9 flare (peaking around 14:30 UT in the soft-X-ray flux) and a halo CME (appearing around 14:12 UT in SOHO/LASCO C2) eruptions occurred on 2012 June 14, followed by an ICME/MC passage at 1 au during June 16–17 (James et al. 2017). In addition to multiview remote-sensing observations from SDO, SOHO, and STEREO A and B spacecraft, the ICME also passed the VEX spacecraft near Venus at a heliocentric distance $r_h \approx 0.7$ au, when VEX was nearly radially aligned with the Sun–Earth line (Kubicka et al. 2016; Chi et al. 2020).

Figure 1 shows the relative locations of multiple spacecraft on the ecliptic plane for this event. Both STEREO A and B were in approximate quadrature with respect to Earth, which provided side views toward the eruption of the corresponding CME and allowed for detailed analysis of the CME kinematics (Zhu et al. 2020). The spacecraft near Earth, including ACE and Wind, detected the subsequent ICME/MC, while VEX, located at $r_h \approx 0.7$ au and about 6° away from the Sun-Earth line to the west, also provided magnetic field measurements of the same ICME structure about 1 day earlier. Figures 2 and 3 show the corresponding in situ time-series measurements at the Wind and VEX spacecraft, respectively. At Wind, both the magnetic field $\boldsymbol{B}$ and solar wind plasma parameters, including flow velocity $\boldsymbol{V}$ (all in the GSE (Geocentric Solar Ecliptic) coordinate) are used for our analysis. In Figure 2, several selected parameters are shown, including the suprathermal electron pitch angle distribution (ePAD) for the 290 eV energy channel. The magnetic field magnitude reaches nearly 40 nT at maximum, and the field components exhibit signatures of rotation within the marked interval. The solar wind speed shows a gradual decrease from $\sim$500 to $\sim$400 km s^{-1}. The effect of such a change will be examined in Section 2.2. The
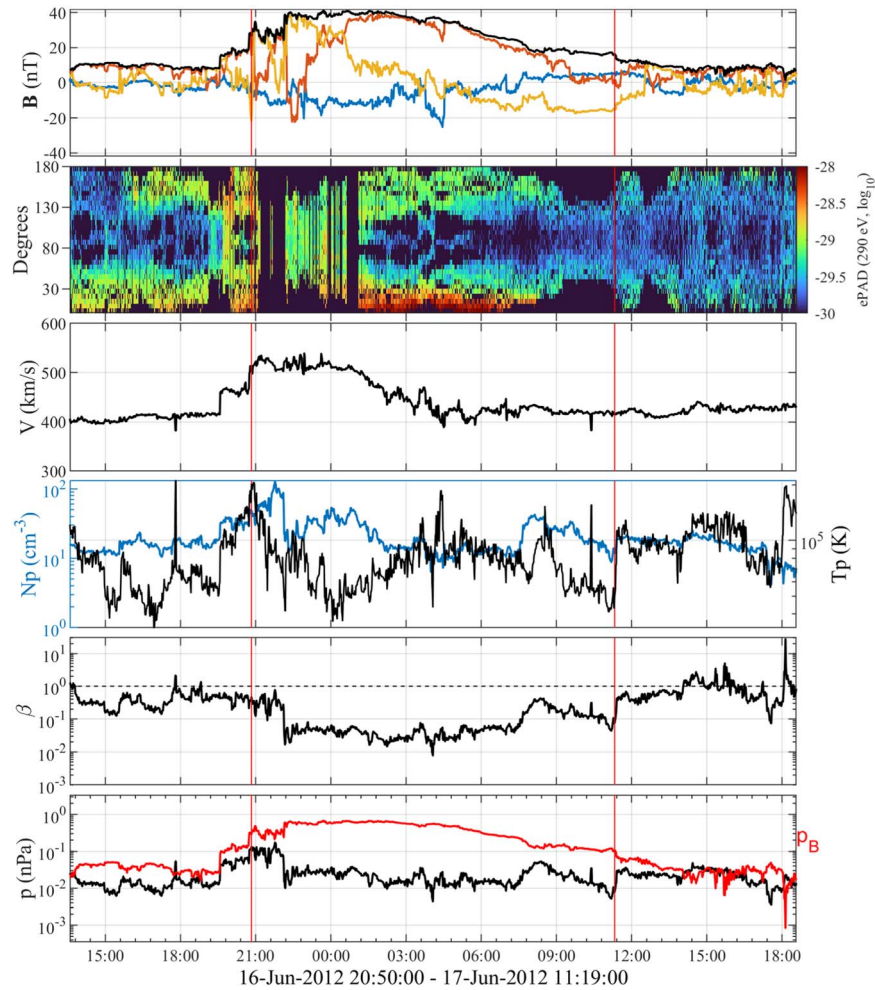
Figure 2. In situ time-series measurements of magnetic field and plasma parameters from the Wind spacecraft. From the top to bottom panels are the magnetic field components in the GSE-*X* (blue), *Y* (red), and *Z* (gold) coordinates, and magnitude (black), the ePAD at 290 eV energy channel, the solar wind speed, the proton density and temperature, the proton β, and the corresponding proton pressure (black) and the magnetic pressure (red). The vertical lines mark the MC interval given beneath the bottom panel for analysis.
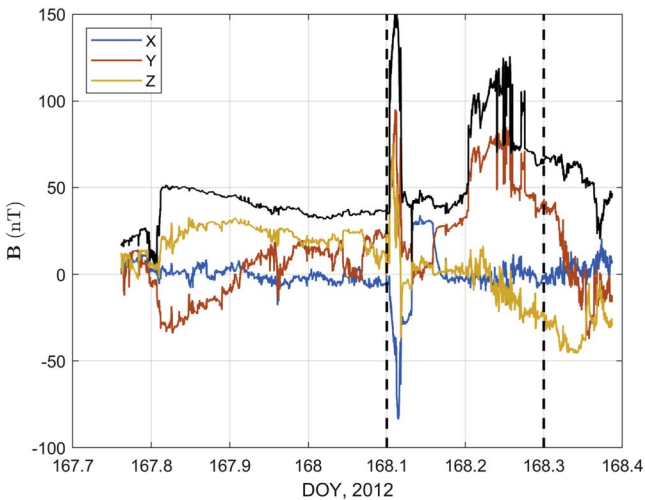
Figure 3. The time series of magnetic field components and magnitude (black) in the Venus Solar Orbital coordinates (the equivalence of the GSE coordinate system defined for Venus) for the interval of the MC passage at Venus during 2012 June 15–16, approximately between DOY 167.7 and 168.4. The dashed lines mark the interval approximately between DOY 168.1 and 168.3 when VEX exited to a different regime (likely the Venusian magnetosphere) from the solar wind. See the text for details.

proton density and temperature vary with periods of depressed proton temperature within the interval. The resulting proton pressure displays little overall variation, but is significantly lower than the corresponding magnetic pressure, which results in significantly depressed proton β, with an average value of 0.10 within the marked interval. Therefore, we identify the marked interval as the passage of an MC and select the corresponding data segments with 1 minute resolution for the subsequent analysis. At VEX, only the magnetic field measurements were available and occasionally contaminated by the Venusian magnetic field, as indicated by large excursions of field magnitudes exceeding, e.g., 80 nT, due to possible bow shock crossings (Xu et al. 2019). Based on the timing analysis (see Section 2.3), the passage of the ICME most likely began around DOY 167.8 with the field magnitude reaching about 50 nT, larger than the maximum magnitude at 1 au. The dashed lines mark the interval bounded by possible bow shock crossings, as indicated by the large magnitude of the magnetic field and the associated frequent and abrupt changes, unlike solar wind behavior. In Section 2.3, this marked time interval is therefore excluded from the correlative comparison with the MC model result derived from the Wind spacecraft measurements.

It is worth noting that from an ICME catalog compiled by Chi et al. (2016) for the years 1995–2015 based on Wind and ACE spacecraft in situ measurements, the distribution of the average magnetic field intensity within the identified ICMEs spans a range between a few nT to more than 37 nT, peaking around the mean value of ∼10 nT. An average magnetic field magnitude greater than 25 nT lies in the tail portion of the distribution with only a handful of such events (<10 out of a total number of nearly 500 events), indicating rare occurrences. This MC event has an average magnetic field magnitude of 29 nT and falls within that range with a strong magnetic field. It was noted by Shen et al. (2021) that this event is among "the top four strongest ICME [sic] in magnetic field strength, according to their ICME catalog.[7]" This fact is consistent with our identified connection of this MC flux rope structure with the MFR rooted in strong magnetic field regions with opposite polarities on the Sun prior to the main flare (M1.9) eruption, as elucidated by Wang et al. (2019). It was found that the average vertical magnetic field strength for the identified positive and negative polarity footpoint regions was 1555 ± 35 G and -710 ± 45 G, respectively. We will further interpret such a connection in Section 3.

2.2. A Quasi-3D MC Model: Freidberg Solution

For the analysis of the MC interval by employing the Wind spacecraft in situ data, we apply a newly developed approach (Hu et al. 2021a), the optimal fitting to the Freidberg solution (FS), which describes a quasi-3D magnetic field configuration. As given below, the three magnetic field components of the FS model in cylindrical coordinates (r, θ, z) satisfy the LFFF formulation, $\nabla \times \boldsymbol{B} = \alpha \boldsymbol{B}$ ($\alpha \equiv$ const.), but allow variations in all three spatial dimensions (Freidberg 2014),

$$\frac{B_z(\boldsymbol{r})}{B_{z0}} = J_0(\alpha r) + C J_1(lr)\cos(\theta + kz), \tag{1}$$

$$\frac{B_\theta(\boldsymbol{r})}{B_{z0}} = J_1(\alpha r) - \frac{C}{l}$$
$$\times \left[\alpha J_1'(lr) + \frac{k}{lr} J_1(lr) \right]\cos(\theta + kz), \tag{2}$$

$$\frac{B_r(\boldsymbol{r})}{B_{z0}} = -\frac{C}{l}\left[k_1'(lr) + \frac{\alpha}{lr}J_1(lr) \right]\sin(\theta + kz). \tag{3}$$

Here, the constant force-free parameter is denoted as α. Additional constant parameters are C, k, and $l = \sqrt{\alpha^2 - k^2}$. The normalization constant B_{z0} is predetermined and taken as the maximum magnitude among all three magnetic field components within the MC interval. The functions, J_0 and J_1, are the usual Bessel functions of the first kind of order 0 and 1, respectively. It is clear that the amplitudes of variations in θ and z (both periodic but adding 3D features) are controlled by the parameter C. For $C \equiv 0$, it reduces to the commonly known Lundquist solution (Lundquist 1950) with only an r dependence.

An optimal fitting between the measured magnetic field components and those yielded by the analytic solution represented by Equations (1)–(3) along the spacecraft path across the MC structure is performed to derive the set of free parameters. They include C, k, and α, and additionally the

_____
[7] http://space.ustc.edu.cn/dreams/wind_icmes/; See also Chi et al. (2016).

orientation of the local cylindrical axis z. An algorithm, following the least-squares minimization approach described by Press et al. (2007), including measurement uncertainty estimates, has been implemented and applied to a few event studies (Hu et al. 2021a; Hu 2021). It has succeeded in yielding a minimum reduced χ^2 value around 1, and the associated *goodness-of-fit* metric $Q > 10^{-3}$, to be considered acceptable (Press et al. 2007).

For this MC interval, the average proton β is about 0.10. A reference frame in which the structure appears to be stationary is determined as the deHoffman-Teller (HT) frame with a constant velocity $\boldsymbol{V}_{\mathrm{HT}} = [-467.12, -9.41, -20.76]$ km s^{-1} in the GSE coordinate system based on Wind spacecraft in situ measurements (see Hu 2021 for details on the justification for the use of $\boldsymbol{V}_{\mathrm{HT}}$ and the associated HT analysis). In short, in such a frame, the spacecraft is moving across the structure with the velocity $-\boldsymbol{V}_{\mathrm{HT}}$. The ratio between the remaining flow $\boldsymbol{v}' = \boldsymbol{V} - \boldsymbol{V}_{\mathrm{HT}}$ and the local Alfvén velocity is evaluated by the slope (the so-called Walén slope) of the regression line between the components of the two velocities, as an indication of the relative importance of the inertial force compared with the Lorentz force. For this event interval, the Walén slope is -0.13 with a magnitude of much less than 1. Therefore, the inertial force can be considered negligible and a force-free equilibrium is considered valid.

Table 1 summarizes the main fitting parameters and derived quantities, where the parameters k and α become dimensionless by multiplying a normalization length a (Hu 2021). The orientation of the z-axis is expressed in terms of the two directional angles, and the axial magnetic flux Φ_z is obtained over the cross-section plane perpendicular to $\hat{z}$ within an area with $B_z > 0$ (Hu 2021). For $\alpha > 0$, it has a positive sign of helicity (or right-handed chirality). The dimensionless parameter α is related to a twist number $\tau_0 = \alpha/2$, the number of twists for a field line of length $2\pi a$, following Liu et al. (2016), for such an LFFF configuration with a constant α. Namely, the twist number for a field line of length L is calculated by the following line integral along each individual field line:

$$T_w = \int_L \frac{(\nabla \times \mathbf{B}) \cdot \mathbf{B}}{4\pi B^2} dl$$
$$= \frac{\alpha L}{4\pi} \propto L \quad (\alpha \equiv \text{const}). \tag{4}$$

By applying a length normalization, i.e., replacing αa by α, $\tau_0 = \alpha/2$ for $L = 2\pi a$ is obtained. It can be scaled for any field lines of arbitrary lengths in the configuration represented by the FS model.

In practice, we usually choose a number of different intervals based on subjective and multiple criteria. Then one interval is selected by weighing the following conditions in the analysis: (1) being as large as possible, (2) bounded by prominent signatures in one or more of these parameters: $\boldsymbol{B}$, $\boldsymbol{V}$, T_p, and β, and (3) acceptable fitting results (the minimum reduced $\chi^2 \leqslant 2$) subject to the physical constraint of axial magnetic flux no larger than 10^{22} Mx (Hu et al. 2014). The merit of presenting an interval as large as possible is that any similar results obtained for shorter intervals enclosed by the larger one are also included in the presentations. For example, for a shorter interval starting about 1 hr later than the one presented in Figure 2, the FS model fitting yielded the optimal set of parameters, $[C, k, \alpha] = [-0.5368, -1.262, 2.774]$, and the z-axis orientation that is about $15°$ away from the z-axis given in Table 1, which are all well within the ranges of the

Table 1
Summary of the Geometrical and Physical Parameters for the MC from the FS Model Based on Wind Spacecraft Measurements

B_{z0} (nT)	C	k	α	$\hat{z} = (\delta, \phi)^{a}$	Φ_z (Mx)	Chirality
38	-0.7138	-1.286	2.626	(56, 150)	8.0–14	+
	± 0.3518	± 0.5123	± 0.2766	$\pm(10,15)$	$\times 10^{20}$	(right-handed)

Note.
[a] The polar angle δ from the ecliptic north, and the azimuthal angle ϕ measured from GSE-X toward GSE-Y axes, both in degrees.

corresponding uncertainties for the optimal solution obtained for the larger interval. Therefore, the results for the shorter interval can be regarded as the same as that to be presented.

Figure 4 formally shows the result of the optimal fitting to the FS formulation given by Equations (1)–(3) for the magnetic field measurements downsampled to about a 30 minute resolution with uncertainties along the Wind spacecraft path. The minimum reduced χ^2 value is 1.44, and the corresponding $Q = 0.00687$. The set of main parameters as presented in Table 1 represents the optimal output from the fitting procedure with uncertainty estimates based on 90% confidence limits (Press et al. 2007; Hu et al. 2021b). The parameter C has a magnitude close to 1, indicating significant deviation from a cylindrically symmetric configuration, as we will demonstrate below. The orientation of the z-axis in directional angles (δ, ϕ) is obtained in the same procedure with uncertainties. In turn, the axial magnetic flux Φ_z is estimated to be 8.0–14 $\times 10^{20}$ Mx, mainly subject to the uncertainty in the z-axis orientation.

Figure 5 shows a cross section of the fitted FS model at (arbitrarily selected) $z = 0$. A boundary (closed in this view) is chosen where $B_z = 0$ as illustrated by the thick dotted magenta curve, within which the axial field B_z is positive, as indicated by the color bar. This solution has a single dominant and positive B_z polarity. Note that for this solution, unlike the 2D GS model, the transverse field as represented by the blue arrows is no longer tangential to the contours of B_z, and such a cross-section map changes with z. Both the Wind and VEX spacecraft paths are projected onto this view, although neither of the paths lies entirely on this plane. A correlative analysis between the FS model prediction along the VEX spacecraft path and the actual measurements of the magnetic field will be presented in Section 2.3.

The 3D nature of the FS model result is better illustrated by Figure 6, where a 3D view of the field-line configuration from the perspective of Earth toward the Sun is given. The main flux bundle in orange is rooted on the bottom cross-section plane with a major positive B_z polarity and is winding upward along the positive z-axis direction. It displays a writhe in the body of the flux bundle, which gives rise to the 3D feature of the magnetic field configuration. In the same view, Figure 7 presents the selected field lines intercepting the Wind space-craft path and color coded by the corresponding B_z field components with the same scales indicated by the color bar in Figure 5, except for the two red lines. Along the Wind spacecraft path, from the beginning to the end, the B_z component changes from positive to negative values. This indicates the corresponding changes in the field line directions from going upward to downward, with respect to the bottom plane, as the color of the field lines transitions from bright gold to blue. The main flux bundle or band with gold to light blue colors twists collectively along the z dimension. Overall there lacks a central straight field line in this configuration. This is further illustrated by highlighting the two field lines in red,
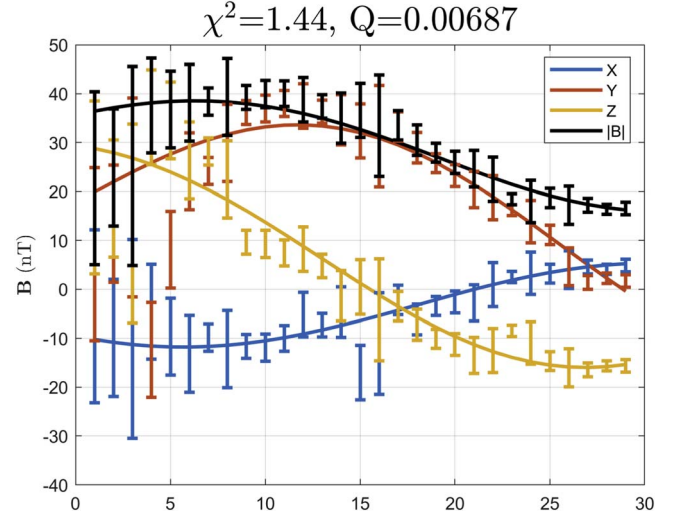

Figure 4. The optimal fitting result for the MC interval by the FS model along the Wind spacecraft path (horizontal axis shows the indices of the data points). The magnetic field components and magnitude are shown for both the Wind spacecraft measurements with uncertainties as discrete error bars and the corresponding FS model output by the solid curves (see the legend), both in GSE coordinates. The minimum reduced χ^2 value and the goodness-of-fit parameter Q are indicated on top.
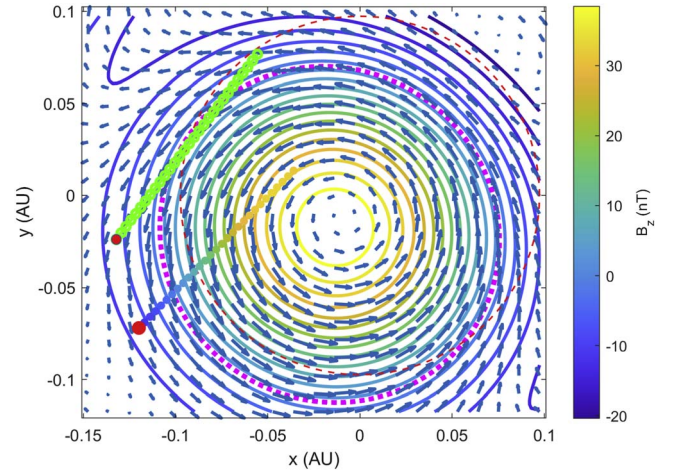
Figure 5. The magnetic field configuration on one cross section of the FS model with the optimal fitting parameters. The blue arrows represent the transverse field components, and the axial field component B_z is denoted by the color contours with color scales indicated by the color bar. The thick dotted magenta curve marks the boundary where $B_z = 0$. The thin red dashed circle is centered at the origin with the radius $a = 0.097$ au. The Wind and VEX spacecraft paths are projected separately by two groups of colored dots along two straight lines, with the former colored by the corresponding B_z values and the latter in green. The endpoint along each path is marked in red.

which connect to two *central* locations with the maximum B_z values at two different cross-section planes (i.e., with two different z values). Overall, the field-line configuration
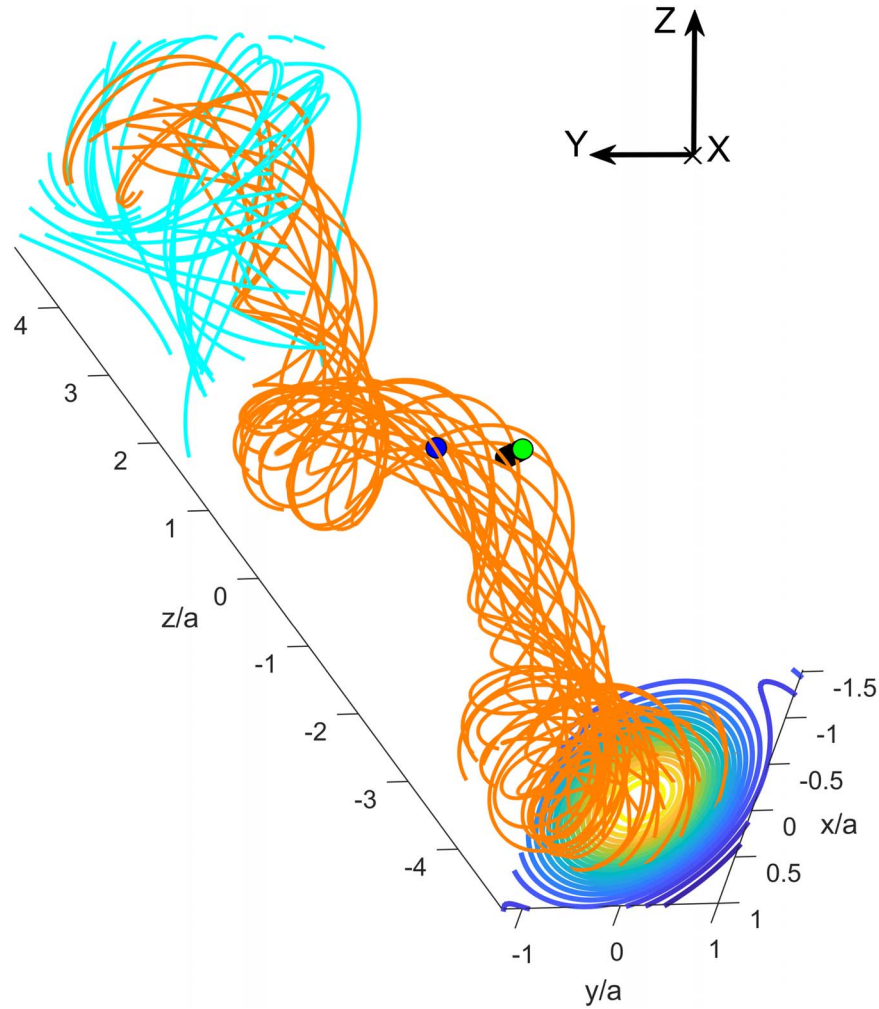
Figure 6. A field-line plot in a Cartesian volume of the (x, y, z) coordinates and in a view toward the Sun along the Wind spacecraft path. The ecliptic north is straight upward, and the east–west direction is horizontal, as indicated by the corresponding GSE X, Y, and Z coordinates. The orange lines are the field lines originating from the bottom plane where the contours of B_z are shown. The cyan lines originate from the top plane (not shown) and are going downward as well as out of the volume. The blue and green dots represent the Wind and VEX spacecraft paths in this view, respectively.

showcases a *twisted-ribbon* type of topology with a knotted appearance in this view.

2.3. Correlation with VEX Measurements

Both the Wind and VEX spacecraft paths cross the main flux bundle, as indicated in Figures 5 and 6, by taking into account a nominal time shift between the two spacecraft, due to the relatively small separations in both heliocentric distances and longitudes. The time shift is calculated by considering a constant propagating speed of the structure at $|V_{HT}|$. By omitting the temporal change of the structure during the propagation, we compare the magnetic field components along the VEX spacecraft path derived from the FS model based on the Wind spacecraft measurements with the actual VEX data shown in Figure 3. The comparison including the magnetic field magnitude is given in Figure 8 with the VEX data downsampled to about a 30 minute resolution with uncertainty estimates. The component-wise correlation is displayed in the right panel of Figure 8, yielding a linear correlation coefficient $cc = 0.86$, for the two data sets excluding the data points between the vertical dashed lines, many reaching large magnitudes beyond 40 nT, as shown in the left panel. Those

are likely due to the contamination from the Venusian magnetosphere as discussed in Section 2.1.

3. Connection to Solar MFR Properties and Interpretation

As we have discussed, based on prior studies (e.g., James et al. 2017) and the fact that the MC as detected at 1 au possesses a significant amount of magnetic flux with an unusually large magnetic field magnitude, the correspondence of the MC analyzed in Section 2 to the preexisting MFR identified by Wang et al. (2019) is one likely scenario. We base our comparison of a handful of characteristic physical properties between the MC and the solar source region on this connection. Again we intend to illuminate an alternative and perhaps unusual scenario that goes beyond the standard view as we described in Section 1.

Table 2 summarizes the selected physical properties, mainly concerning the magnetic field topology and flux contents for both the MC and the source region, including the preexisting MFR as reported by Wang et al. (2019). According to Wang et al. (2019), "The evolution of the MFR is observed by STEREO and SDO from multiple viewpoints. From STEREO's perspective, the MFR starts to rise slowly above the limb 5 hr before it erupts as a halo CME on 2012 June 14.
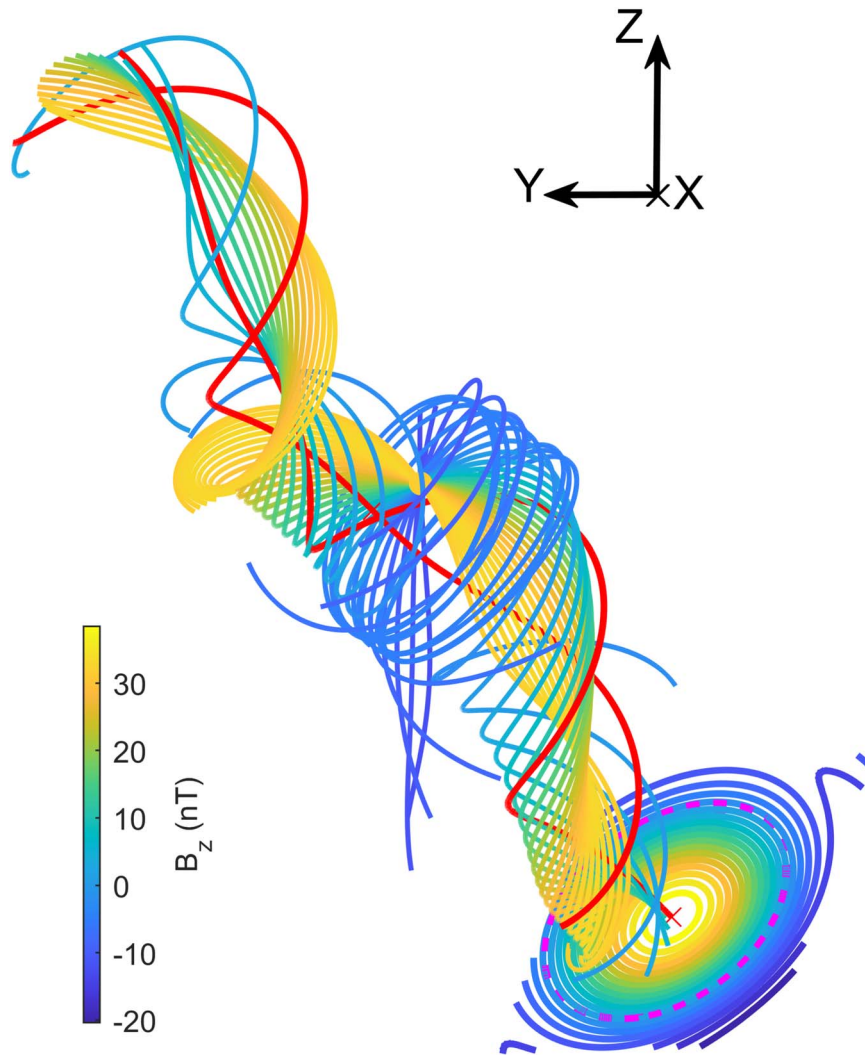
Figure 7. Selected field lines crossing the Wind spacecraft path in exactly the same coordinates and view angle as Figure 6 and color coded by the corresponding B_z values with the same color bar as Figure 5. Two thicker lines in red highlight the 3D nature of the configuration: one is rooted on the bottom plane where the contours of B_z are shown, and starts from the point with the maximum B_z; the other crosses the point of maximum B_z on a different plane, as shown in Figure 5. They apparently are not straight lines.

In SDO observations, conjugate dimmings develop on the disk, simultaneously with the gradual expansion of the MFR, suggesting that the dimmings map the MFR's feet. The evolution comprises a two-stage gradual expansion followed by another stage of rapid acceleration/eruption." For several hours before the M1.9 flare eruption, coronal dimming was observed and analyzed from AIA 304 Å images; it was accompanied by the slow rising of coronal structures observed in STEREO. These signatures indicate the slow rise of a preexisting flux rope prior to its eruption, and its feet are mapped in the pre-eruption dimming regions. These dimming regions were well confined to the conjugate feet of the preexisting MFR and maintained through the flare onset. Therefore, the total magnetic flux measured in these regions by Wang et al. (2019) with small uncertainties as cited here in Table 2 is considered to be the preexisting total flux of the flux rope before magnetic reconnection associated with the M1.9 flare. For the subsequent M1.9 flare eruption, the associated flare ribbons swept through the two feet of the identified preexisting MFR (see Figure 9), which was believed to conform to a scenario of *leg–leg* reconnection.

The reconnection flux is derived from the temporal and spatial evolution of flare ribbons from our own analysis following the standard approach of Qiu et al. (2004, 2010). Such analysis results are presented in Figure 9. Similar results for the reconnection flux were also provided by Wang et al. (2019). Depending on how the threshold conditions for the brightening ribbon pixels are chosen, and other factors, the results may differ slightly. Especially considering the time duration during which the brightening pixels are counted and included, the final accumulative magnetic flux enclosed by the areas swept by the brightened ribbon pixels may differ among separate studies. Generally speaking, the longer the duration, the larger the reconnection flux (taken as equivalent to the ribbon flux) becomes. We finish the measurement of the reconnection flux at a time earlier than Wang et al. (2019) when the ribbons started to spread outside of the boundaries of the preexisting MFR's footpoint regions (the red contours) in Figure 9(b). The accumulative reconnection flux shown in Figure 9(c) has gone through a phase of rapid increase and is changing more gradually at later times, coinciding with the change in the reconnection rate.
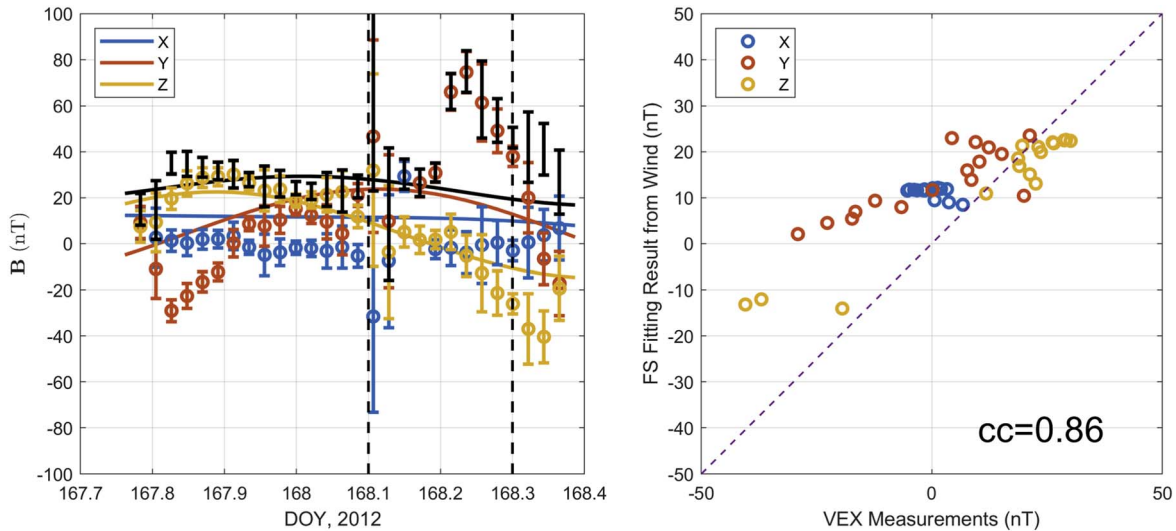
Figure 8. Left panel: time series of the magnetic field components (see the legend) and magnitude (black) at VEX, including the VEX measurements represented by error bars and the FS model output by smooth curves. The pair of dashed lines mark the period of close Venus encounter, which is excluded from the results of the analysis shown in the right panel. Right panel: the corresponding scatter plot of the two sets of field components, yielding a correlation coefficient cc = 0.86. The dashed line indicates the one-to-one diagonal line.

Table 2
Summary of Results from Both Remote-sensing and In Situ Data Analyses of the Source Region and the Corresponding MC Properties

Parameters (fluxes in 10^{20} Mx)	Source Region[a]	In Situ MC Model 3D (FS)
Axial magnetic flux Φ_z	(+)42 ± 1, (−)30 ± 1	8.0–14
Total twist number τ	~2	1.9–2.4/au
Magnetic helicity (10^{42} Mx²)	6–10	1.6–3.5 /au
Reconnection flux	(+)22 ± 4.7, (−)21 ± 5.3	⋯

Note.
[a] The first three rows are estimates from Wang et al. (2019) for the preexisting MFR, including the axial magnetic fluxes for the positive (+) and negative (−) polarity footpoint regions based on dimming and magnetograph measurements.

The results from Wang et al. (2019) indicate that the preexisting MFR contains a significant amount of flux with both footpoints rooted in regions with a strong but opposite polarity magnetic field. Considering that for the time period shown in Figure 9, the flare ribbons swept through both footpoint regions while largely confined within the boundaries of the preexisting MFR footpoints as marked. The reconnection flux has to correspond to the reconnected flux between the field lines belonging to the preexisting MFR. This is consistent with the reconnection sequence identified as *rope–rope* to *rope-flare-loop* type (or "rr-rf" in short) by Aulanier & Dudík (2019, see Figure 4 therein). Simply put, such a scenario may be traced back to the earlier schematics by Gosling et al. (1995) where the reconnection between two legs of adjacent loops, each leg belonging to a different loop, results in one unit of axial flux being removed due to the disconnection of one pair of footpoints from the loop structure (or the flux rope) above to form a closed flare loop below. Therefore, a reduction in the axial (toroidal) magnetic flux of the MFR by the amount of the reconnection flux should result.

This leads to an expected remaining axial magnetic flux of the erupted flux rope in the range of 9–20 × 10^{20} Mx (by subtracting the last row from the first row in the middle column

of Table 2) with about $\gtrsim$20% uncertainty for this event. The erupted flux rope was later detected by the Wind spacecraft at 1 au with in situ measurements and the FS modeling results yield an axial flux, 8.0–14 × 10^{20} Mx, which overlaps with the range of the anticipated value. The twist number estimates, on average, do not change significantly, although the total twist number estimate for the FS model is still subject to large uncertainty in the field-line length. The magnetic helicity contents are approximately of the same order of magnitude for the preexisting MFR and in situ MC model results. Moreover, for this event, the connectivity of field lines in the MC flux rope back to the positive polarity footpoint region on the Sun is better maintained, as implied by a larger amount of remaining magnetic flux in the positive polarity footpoint region. This seems to be consistent with the ePAD data where the relative enhancement of the streaming suprathermal electrons is more pronounced at 0° PA within the MC interval shown in the second panel of Figure 2. This signature, corresponding to unidirectional streaming electrons (see, e.g., Gosling et al. 1995), generally indicates stronger connectivity of only one end of a field line to the positive polarity footpoint region.

Figure 10(a) shows the typical set of time-varying profiles of the speed v, and acceleration a of the associated CME (Zhu et al. 2020), and the product av as a possible proxy to the rate of change of kinetic energy (assuming little change in CME mass). Figures 10(b) and (c) show the corresponding measurements of the accumulative reconnection flux, the rate of change of the reconnection flux, the soft-X-ray flux, and its temporal derivative, respectively. It shows a general pattern of coincidence in the peaks of the acceleration, the reconnection rate, and the rate of change of the soft-X-ray flux, which has been demonstrated for many flare/CME events (e.g., Zhu et al. 2020). The peak in the product av seems to slightly lag behind the other peaks (see, e.g., Karpen et al. 2012). The latest numerical simulation study by Jiang et al. (2021a) showed better coincidence between the peak of the rate of change in kinetic energy and that in the reconnection rate. The overall temporal profiles generally coincide with each other among the
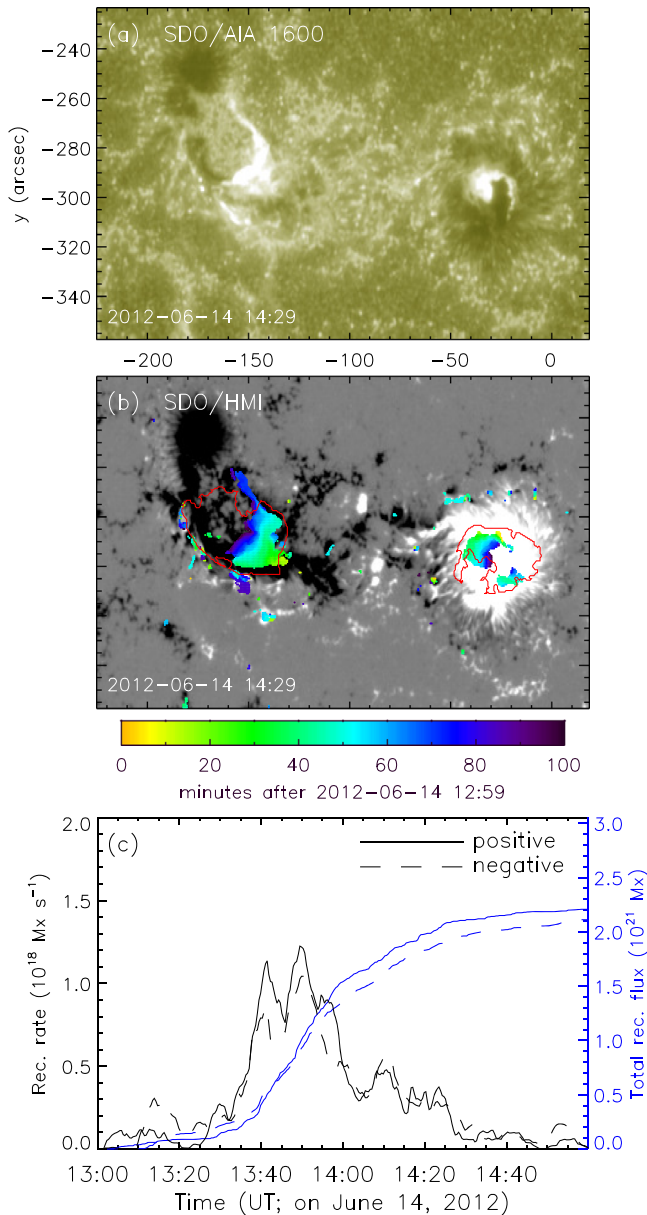
Figure 9. The magnetic reconnection properties derived from the associated flare ribbon morphology: (a) the SDO/AIA 1600 Å image at the time of the peak of the M1.9 flare, (b) the corresponding HMI magnetogram with the brightened flare ribbon pixels overlaid and color coded by the elapsed time as indicated by the color bar, and (c) the corresponding measured accumulative reconnection flux and the reconnection rate for the positive and negative polarities, respectively. In panel (b), the red contours mark the boundaries of the positive and negative polarity footpoint regions of the preexisting MFR identified by Wang et al. (2019).

corresponding changes in the reconnection rate, the CME acceleration, and the time derivative of the soft-X-ray flux.

In summary, based on these quantitative analysis results, we offer the main interpretation such that the reconnection associated with the M1.9 flare on 2012 June 14 reduces the axial flux of the preexisting MFR upon eruption by around 50%, while the MFR-CME kinematic behavior is largely unaffected.

4. Conclusions and Discussion

In conclusion, we have carried out an additional quantitative analysis of the flare-CME-ICME/MC event during 2012 June 14–17, especially by performing an analysis of the MC configuration through a newly developed quasi-3D FS fitting approach. The MC observed by the Wind spacecraft possesses an unusually strong magnetic field magnitude (with the maximum reaching 40 nT), which was also crossed by the VEX spacecraft at $r_h \approx 0.7$ au and 6° west of the Sun–Earth line. The optimal fitting of the FS model to the Wind in situ magnetic field measurements yields a minimum reduced $\chi^2 \approx 1.44$. The field-line configuration shows an indication of writhe of the main flux bundle winding in the direction $\hat{z} = (56°, 150°)$ in terms of the polar and azimuthal angles in GSE coordinates. Such a feature is not present in either 1D or 2D flux rope models. The VEX spacecraft crossed the main flux bundle to the west near the ecliptic from the point of view from Earth toward the Sun. The spatial variations from the Wind spacecraft path to that of VEX are significant and intrinsically 3D based on the FS model output. A comparison of the magnetic field components between the FS model output along the VEX spacecraft path and the actual time series data yields a correlation coefficient of cc = 0.86.

Based on the uncertainty estimates for the fitting parameters of the FS model, the axial magnetic flux (all in units of 10^{20} Mx hereafter) of the MC flux rope is estimated to be 8.0–14. A preexisting MFR was identified in Wang et al. (2019) with two footpoint regions rooted in strong magnetic polarity regions and the axial flux amounting to 42 and 30 for the positive and negative polarities, respectively. The subsequent M1.9 flare exhibited brightened ribbons mostly confined within the boundaries of the identified preexisting MFR footpoint regions. The corresponding accumulative reconnection flux reaches 22 ± 4.7 and 21 ± 5.3 for the positive and negative polarities, respectively. This implies a reduction in the axial magnetic flux of the preexisting MFR by the total amount of the reconnection flux. Therefore, the erupted CME flux rope accompanying the flare should contain the amount of axial flux in the range of 9–20 with uncertainties, which agrees with the range of the estimated axial flux of the MC flux rope. This result supports the scenario of the reconnection sequence between the field lines of the preexisting MFR near the two legs, as envisaged by Aulanier & Dudík (2019). In addition, the kinematics of the accompanying CME as analyzed through coronagraphic measurements show little distinction from the general pattern in terms of the coincidence among the peaks of the CME acceleration, the reconnection rate, and the rate of change of the soft-X-ray flux. In other words, such a presumably unusual process of the removal of the axial magnetic flux from the erupting MFR through flare reconnection appears to have little effect on the CME kinematics. The main characteristics remain similar to the other more typical process during which the reconnection flux is injected into the erupting MFR forming the CME (see, e.g., Zhu et al. 2020). Lastly, the ePAD signatures with relatively greater enhancement at 0° PA during the MC interval seem to be consistent with the aforementioned interpretation as well.

The complexity or evolution of a flux rope topology is probably not limited to the process of the leg–leg type reconnection only. Additional ribbon brightenings after the main sequence may correspond to other types of reconnection not resulting in the deduction of axial flux. For example, the
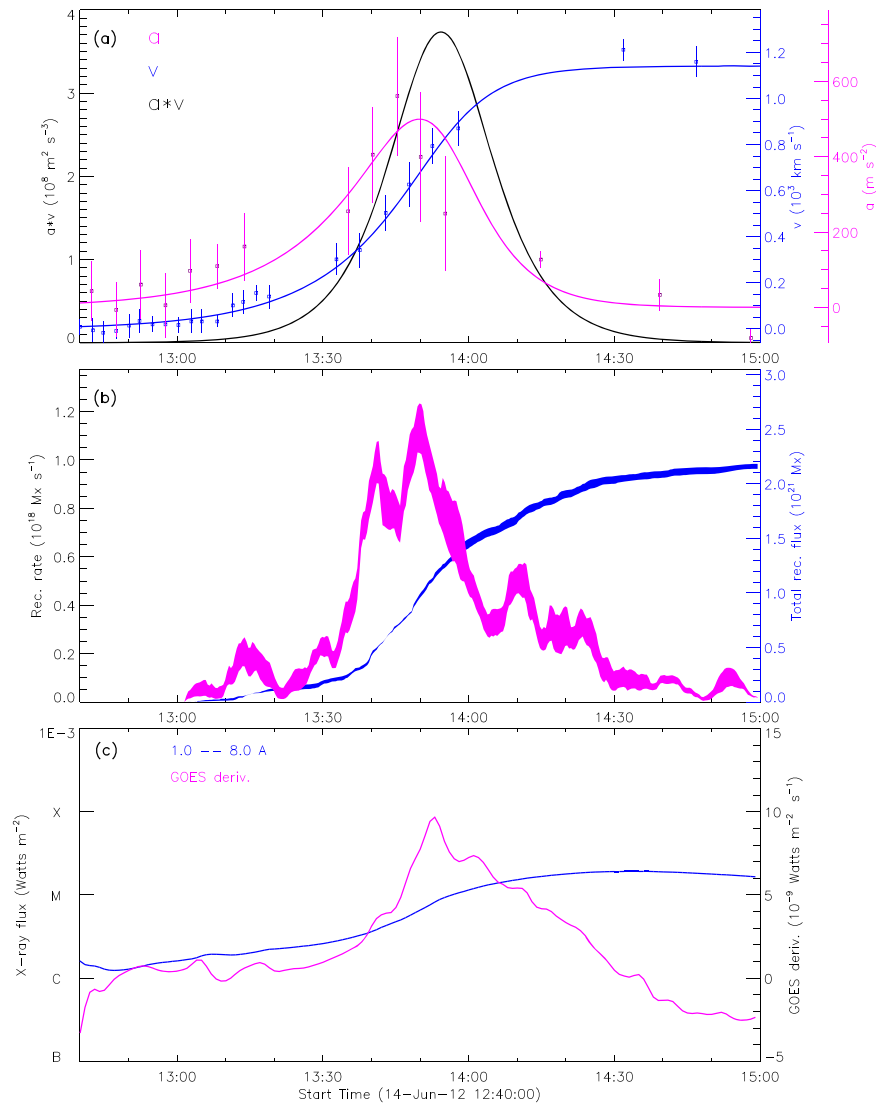
Figure 10. Temporal variations of (a) the CME speed v, acceleration a, and the product av, (b) the corresponding reconnection flux and reconnection rate derived from flare ribbons (line thickness represents the range of uncertainty estimates), and (c) the corresponding GOES soft-X-ray flux and its derivative.

latest numerical simulation by Jiang et al. (2021a) demonstrated the buildup of an MFR from magnetic reconnection with the axial flux of the MFR increasing initially in sync with the reconnection flux, then the axial flux started to decrease while the reconnection flux continued to grow. Apparently not all reconnection flux over an extended period of time corresponds to the reduction in the axial flux of the MFR. For example, one recent observational analysis by Xing et al. (2020) on the evolution of the axial flux in identified MFR footpoints showed a modest decrease of about 10%–20%. The reconnection in later stages may instead correspond to an interchange type of reconnection with either open or closed neighboring flux systems, resulting in the disconnection or *drifting* of the MFR footpoints (Zemanová et al. 2019; Aulanier & Dudík 2019) without altering the axial flux, especially when quantified from in situ measurements.

We wish to point out the 3D features of the FS model. Based on Equation (4), the constant parameter α denotes the number of twists per unit length (subject to a constant proportional factor). So the total twist for a single field line is proportional to the product of α and the field-line length L from one end to the other. This will be a finite and unique number for any field line
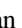
with a finite length. For a straight field line, the twist number becomes arbitrary. As we pointed out, there are no straight field lines in the configuration presented here. This imposes a challenge for defining a *center* of the flux rope to be along a straight field line as we usually do for a 2D configuration (Hu 2017; Hu et al. 2021a). Moreover, a distinction between the field-line twist per unit length and the total twist number has to be made, and it is generally more appropriate and accurate for the latter to be compared with its corresponding solar source region counterpart, e.g., in Table 2. However, such a comparison is not feasible because the current flux rope models based on in situ measurements lack the capability of determining the field-line lengths L. Therefore, the proper evaluation of the total field-line twist based on in situ MC modeling remains challenging. In addition, a 3D field-line configuration also leads to difficulty in defining the poloidal flux of a flux rope, as we discussed in He et al. (2022), simply because of the difficulty in defining a central axis.

We are also aware that James et al. (2018) found a preexisting MFR prior to the eruption of the M1.9 flare through a nonlinear force-free field extrapolation. They succeeded in generating an MFR structure in their solution

by using an HMI vector magnetogram patch around 12:24 UT on 2012 June 14. The amount of axial magnetic flux contained in the MFR is 4×10^{20} Mx, based on their extrapolation result. The total average twist number was estimated to be between 1.35 and 1.88. Based on Table 2, if one assumes that the accumulative reconnection flux were all injected into the erupting CME flux rope, the total axial flux would amount to $\sim 20 \times 10^{20}$ Mx or more, considering uncertainties. This process may comply with the other scenario as discussed in Section 1, although this amount seems to be larger than the upper limit of the range of axial flux contained in the corresponding MC flux rope. It is possible that not all reconnection flux may add to the (axial) flux content of the MC flux rope. However to discern all possible scenarios would require a detailed analysis of reconnection sequence combining flare ribbon morphology and magnetic field topology/connectivity, as attempted by Qiu (2009) for one case study. This will be pursued in future studies. It might also be possible that the MC flux may be reduced during its propagation through the interplanetary space before reaching 1 au, which is beyond the scope of this study.

ORCID iDs

Qiang Hu https://orcid.org/0000-0002-7570-2301
Chunming Zhu https://orcid.org/0000-0003-3218-5487
Jiong Qiu https://orcid.org/0000-0002-2797-744X
Lan K. Jian https://orcid.org/0000-0002-6849-5527
Avijeet Prasad https://orcid.org/0000-0003-0819-464X

References

Amari, T., Canou, A., Aly, J.-J., Delyon, F., & Alauzet, F. 2018, Natur, 554, 211
Aulanier, G., & Dudík, J. 2019, A&A, 621, A72
Burlaga, L. F. 1988, JGR, 93, 7217
Burlaga, L. F. E. 1991, Physics of the Inner Heliosphere II, 152 (Berlin: Springer-Verlag),
Burlaga, L. F., Klein, L., Sheeley, N. R. J., et al. 1982, GeoRL, 9, 1317
Chi, Y., Scott, C., Shen, C., et al. 2020, ApJ, 899, 143
Chi, Y., Shen, C., Wang, Y., et al. 2016, SoPh, 291, 2419
Freidberg, J. P. 2014, Ideal MHD (Cambridge: Cambridge Univ. Press), 546
Gopalswamy, N., Yashiro, S., Akiyama, S., & Xie, H. 2017, SoPh, 292, 65
Gosling, J. T. 1990, GMS, 58, 343
Gosling, J. T., Birn, J., & Hesse, M. 1995, GeoRL, 22, 869
He, W., Hu, Q., Jiang, C., Qiu, J., & Prasad, A. 2022, arXiv:2201.03149
Hu, Q. 2017, ScChD, 60, 1466
Hu, Q. 2021, SoPh, 296, 101
Hu, Q., He, W., Qiu, J., Vourlidas, A., & Zhu, C. 2021a, GeoRL, 48, e90630
Hu, Q., He, W., Zhao, L., & Lu, E. 2021b, FrP, 9, 407
Hu, Q., Qiu, J., Dasgupta, B., Khare, A., & Webb, G. M. 2014, ApJ, 793, 53
Hu, Q., Smith, C. W., Ness, N. F., & Skoug, R. M. 2005, JGR, 110, 9
Hu, Q., & Sonnerup, B. U. Ö. 2001, GeoRL, 28, 467
Hu, Q., & Sonnerup, B. U. Ö. 2002, JGR, 107, 1142
James, A. W., Green, L. M., Palmerio, E., et al. 2017, SoPh, 292, 71
James, A. W., Valori, G., Green, L. M., et al. 2018, ApJL, 855, L16
Jiang, C., Chen, J., Duan, A., et al. 2021a, FrP, 9, 575
Jiang, C., Feng, X., Liu, R., et al. 2021b, NatAs, 5, 1126
Karpen, J. T., Antiochos, S. K., & DeVore, C. R. 2012, ApJ, 760, 81
Kazachenko, M. D., Lynch, B. J., Welsch, B. T., & Sun, X. 2017, ApJ, 845, 49
Kubicka, M., Möstl, C., Amerstorfer, T., et al. 2016, ApJ, 833, 255
Lepping, R. P., Burlaga, L. F., & Jones, J. A. 1990, JGR, 95, 11957
Liu, R. 2020, RAA, 20, 165
Liu, R., Kliem, B., Titov, V. S., et al. 2016, ApJ, 818, 148
Lundquist, S. 1950, Ark. Fys., 2, 361
Longcope, D. W., & Beveridge, C. 2007, ApJ, 669, 621
Möstl, C., Farrugia, C. J., Biernat, H. K., et al. 2009, SoPh, 256, 427
Möstl, C., Miklenic, C., Farrugia, C. J., et al. 2008, AnGeo, 26, 3139
Press, W. H., Teukolsky, S. A., Vetterling, W. T., & Flannery, B. P. 2007, Numerical Recipes in C++: The Art of Scientific Computing (New York: Cambridge Univ. Press)
Priest, E. R., & Longcope, D. W. 2017, SoPh, 292, 25
Qiu, J. 2009, ApJ, 692, 1110
Qiu, J., Hu, Q., Howard, T. A., & Yurchyshyn, V. B. 2007, ApJ, 659, 758
Qiu, J., Liu, W., Hill, N., & Kazachenko, M. 2010, ApJ, 725, 319
Qiu, J., Wang, H., Cheng, C. Z., & Gary, D. E. 2004, ApJ, 604, 900
Shen, C., Chi, Y., Xu, M., & Wang, Y. 2021, FrP, 9, 673
van Ballegooijen, A. A., & Martens, P. C. H. 1989, ApJ, 343, 971
Vourlidas, A. 2014, PPCF, 56, 064001
Wang, W., Liu, R., Wang, Y., et al. 2017, NatCo, 8, 1330
Wang, W., Zhu, C., Qiu, J., et al. 2019, ApJ, 871, 25
Wu, C.-C., Lepping, R. P., & Berdichevsky, D. B. 2021, FrP, 9, 429
Xing, C., Cheng, X., & Ding, M. D. 2020, Innov., 1, 100059
Xing, C., Cheng, X., Qiu, J., et al. 2020, ApJ, 889, 125
Xu, Q., Xu, X., Chang, Q., et al. 2019, ApJ, 876, 84
Zemanová, A., Dudík, J., Aulanier, G., Thalmann, J. K., & Gömöry, P. 2019, ApJ, 883, 96
Zhang, T., Baumjohann, W., Delva, M., et al. 2006, P&SS, 54, 1336
Zhu, C., Qiu, J., Liewer, P., et al. 2020, ApJ, 893, 141
Zurbuchen, T. H., & Richardson, I. G. 2006, SSRv, 123, 31